CHANDRA
X-ray Center 60 Garden St., Cambridge Massachusetts 02138 USA

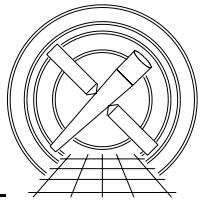

MEMORANDUM

Date: November 26, 2003, Chandra Calibration Workshop
From: Eli Beckerman, Beth Biller, Diab Jerius
Subject: Measurement of Telescope Vignetting with SNR G21.5-0.9
Version: 1.0

Abstract

We present measurements of the *Chandra* vignetting function – the fractional decrease in telescope throughput for off-axis objects – using a sequence of off-axis Chandra observations of the supernova remnant G21.5-0.9. The observations were performed in such a way as to minimize the effects of detector quantum efficiency variations. We compare the results of this SNR with the current models of the vignetting function, which were used to generate the vignetting tables provided in the CALDB.

1 Introduction

Studying the energy-dependent on-orbit vignetting of *Chandra*'s High Resolution Mirror Assembly (HRMA) is made difficult by practical constraints on the observations. Ideally one would use a bright point source, but as we must use ACIS for spectral sensitivity we are limited by pileup. Using the SNR G21.5-0.9 is a reasonable alternative, but spectral variations across the remnant, as well as changes in the relative contributions from different parts of the source due to differential vignetting are complications which must be addressed.

Vignetting functions provided in the CXC Calibration Database (CALDB) give the ratio of off-axis to on-axis effective areas for different off-axis and azimuthal angles at various energies. These values are based on raytraces of the HRMA off-axis performance.

This presentation includes analysis of a series of off-axis observations of G21.5-0.9. We compare the off-axis surface brightnesses of the source to those for the source on-axis.

2 Observations

We examined 9 observations of G21.5-0.9 on the ACIS S3 chip, 6 of which were performed in September 2000, while 3 were taken in May 2003. Some of the earlier observations suffered from background flares and were reobserved as part of the later set. All of the exposure times were between 7.4 and 10.0 ksec. In this analysis, we include results for 5 off-axis angles, all relative to the nominally on-axis observation. Obsids 1838, 1839, 4353, 4354, 4355, and 1843 correspond to off-axis angles θ of $1.3'$, $2.5'$, $5.2'$, $10.2'$, $15.1'$, and $20.1'$. The complete series of vignetting observations is shown in Figure 1.

In order to minimize the effects of detector quantum efficiency, the SIM was translated for each observation so that the remnant always fell on the same part of the ACIS S3 chip. The observation at θ of $20'$ had a background flare throughout and was never re-observed, but we include it (with caution) because it seems the background subtraction might have sufficiently removed the flare.

Figure 2 shows the $20'$ off-axis observation along with the source and background extraction regions. We use the same $0.82'$ radius source aperture for each observation, along with a 10.8 square $'$ rectangle near the edge of the chip for each background.

3 Analysis

Using Obsid 1838 as our on-axis reference image, we can assess the relative on-orbit vignetting of the telescope. Since this "on-axis" observation is actually $1.3'$ off-axis, we cannot make direct comparisons with the vignetting tables in the CALDB. To determine the absolute telescope vignetting, we would need to observe the source perfectly on-axis. Another complication is that the maximum effective area, $A_{\rm eff}$, is not at $\theta = 0$ due to misalignments in the telescope. In this analysis, we determine the ratio of surface brightnesses off-axis to those for

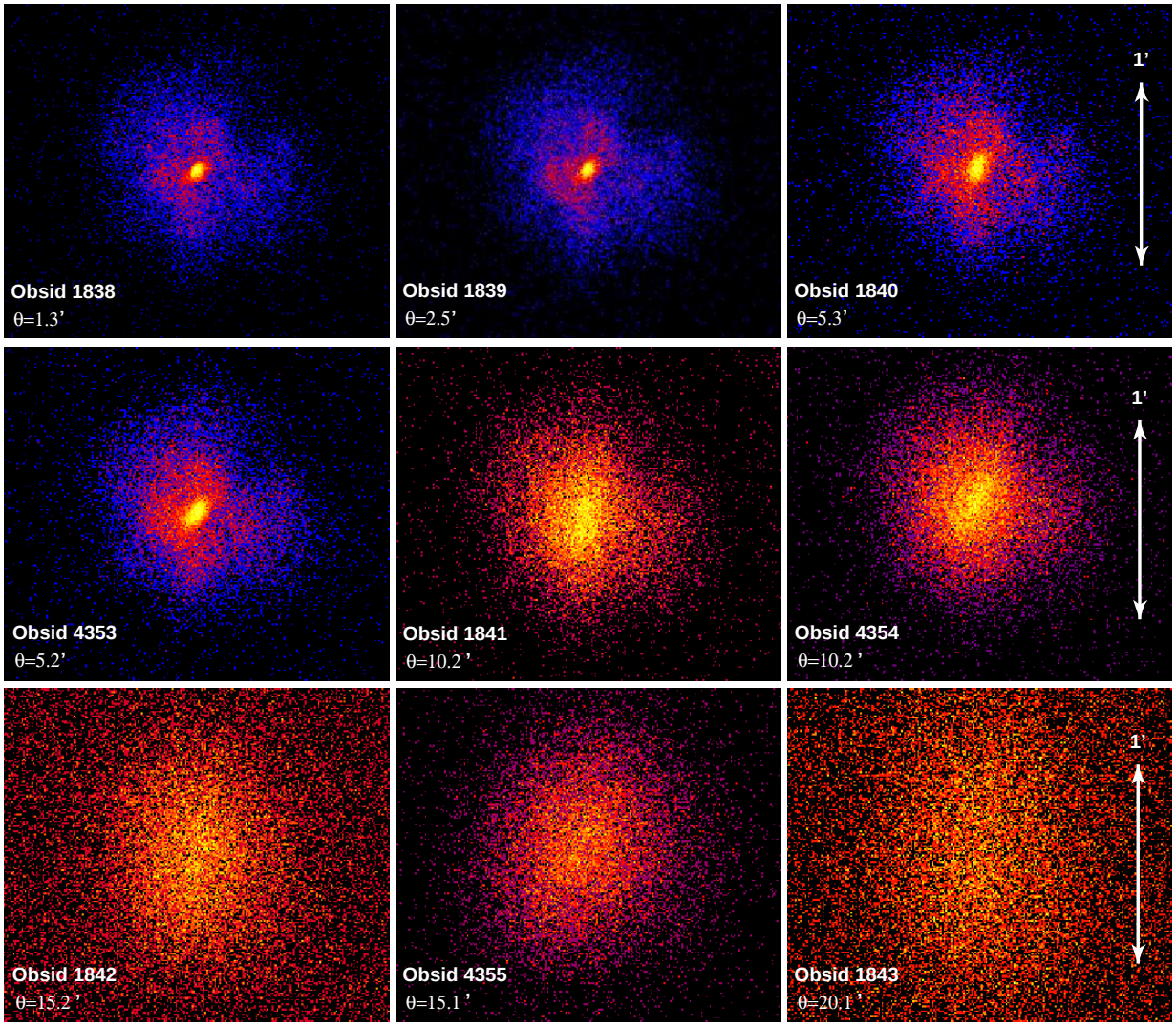

Figure 1: Series of vignetting observations of the SNR G21.5-0.9, out to 20′ off-axis. Obsids 1842 and 1843 suffered from background flares throughout each observation.

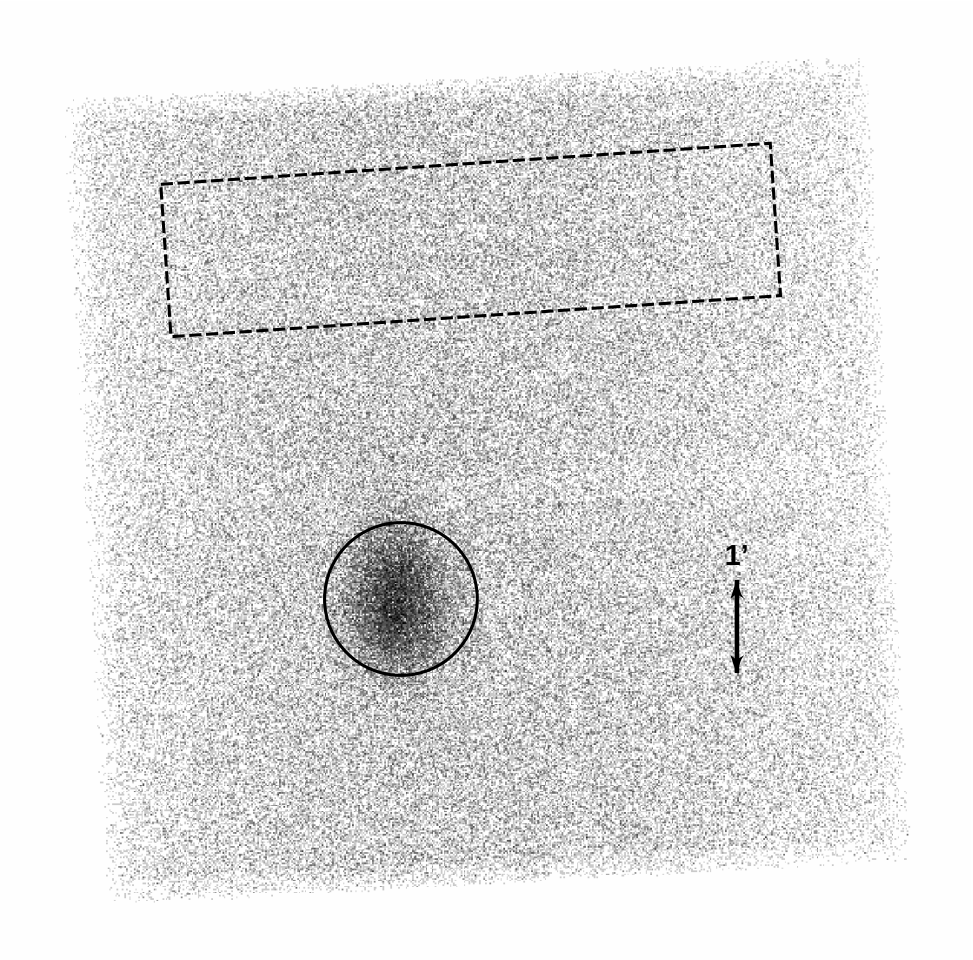

Figure 2: Source and background regions shown for obsid 1843, 20′ off-axis. We use the same 100 pixel radius (1.64′ diameter) apertures to extract source counts for each observation.

the $\theta = 1.3'$ image. Any vignetting corrections applied then take into account that our reference image is slightly off-axis.

We split our observations into energy bands such that our observation with the least signal would have a minimum of 2000 counts in each band. This ensures consistent signal-to-noise in each band, but hampers energy resolution in the low-counts regime above ∼4.5 keV.

We present 3 diagnostic ratios in this study, based on those in an earlier vignetting memo[1]. These are defined in Equations 1 - 3, below. Each equation is the ratio of the surface brightness of the off-axis source to the nearly on-axis ($\theta = 1.3'$) surface brightness.

The raw counts ratio, R_1, represents the observed vignetting function. This contains all effects in the system, including the mirrors, support structures, and detector non-uniformities. It is defined as the ratio of the raw background-subtracted surface brightnesses:

$$R_1 = \frac{\Sigma_{s1} - \Sigma_{b1}}{\Sigma_{s0} - \Sigma_{b0}} = \frac{(\frac{N_{s1}}{A_s t_1} - \frac{N_{b1}}{A_b t_1})}{(\frac{N_{s0}}{A_s t_0} - \frac{N_{b0}}{A_b t_0})} \tag{1}$$

where Σ is the surface brightness, N is the number of counts, A is the area of the region, and t is the effective exposure time. Subscripts 0 and 1 denote on-axis and off-axis, respectively, while s and b refer to source versus background.

The other two quantities are ratios of exposure map corrected fluxes. For these we create exposure maps in a given energy band, weighted by a fit to the on-axis spectrum of the source. We calculate exposure maps for 2 scenarios: a simple quantum effeciency (QE) correction by setting the HRMA effective area (EA) to unity, and a full QE+EA correction, where EA is the HRMA effective area from the CALDB. Both corrections are position- and energy-dependent.

If we use Q to represent the detector quantum efficiency as determined from the CALDB, then R_2 is the ratio of QE-corrected surface brightnesses. If the QE curves are correct, then R_2 is the telescope optical vignetting, which we assume to be pure HRMA vignetting.

$$R_2 = \frac{(\frac{N_{s1}}{A_s Q_{s1} t_1} - \frac{N_{b1}}{A_b Q_{b1} t_1})}{(\frac{N_{s0}}{A_s Q_{s0} t_0} - \frac{N_{b0}}{A_b Q_{b0} t_0})} \tag{2}$$

R_2 should be consistent with R_1 because the observational setup tries to remove QE variations.

If we add in the effective area corrections, then our applied correction is $Q \cdot V$, where V is the vignetting factor for each off-axis location, interpolated from the vignetting tables in the CALDB (which are based on HRMA raytraces). The final diagnostic R_3 is the ratio of QE+EA corrected fluxes. Since these are corrected for all vignetting effects, this ratio would equal unity for an accurate vignetting correction.

$$R_3 = \frac{(\frac{N_{s1}}{A_s Q_{s1} V_{s1} t_1} - \frac{N_{b1}}{A_b Q_{b1} V_{b1} t_1})}{(\frac{N_{s0}}{A_s Q_{s0} V_{s0} t_0} - \frac{N_{b0}}{A_b Q_{b0} V_{b0} t_0})} \tag{3}$$

4 Discussion

Figures 3 – 7 show R_1, R_2, and R_3 for 2.5′, 5.2′, 10.2′, 15.1′, and 20.1′. In almost every case, the QE-corrected vignetting (R_2) matches the observed vignetting (R_1). This validates the assumption that we are effectively avoiding QE effects of the detector by tracking the source with the SIM. Even though the broader image of the off-axis observations samples a larger and thus different part of the detector, the impact of any QE differences is negligible.

The QE+EA corrected vignetting ratio (R_3), as seen in Figures 3 - 7, is consistently greater than unity. While a ratio of 1 would point to an errorless vignetting correction, the values we see could be explained by two general possibilities. First, we might be undercounting the flux in the on-axis observation itself, perhaps because of pileup. The second possible explanation is that the HRMA models are overestimating the vignetting correction for off-axis sources. More rigorous study of this effect will follow, including raytracing the exact locations of these observations to derive HRMA vignetting curves which can be compared more directly.

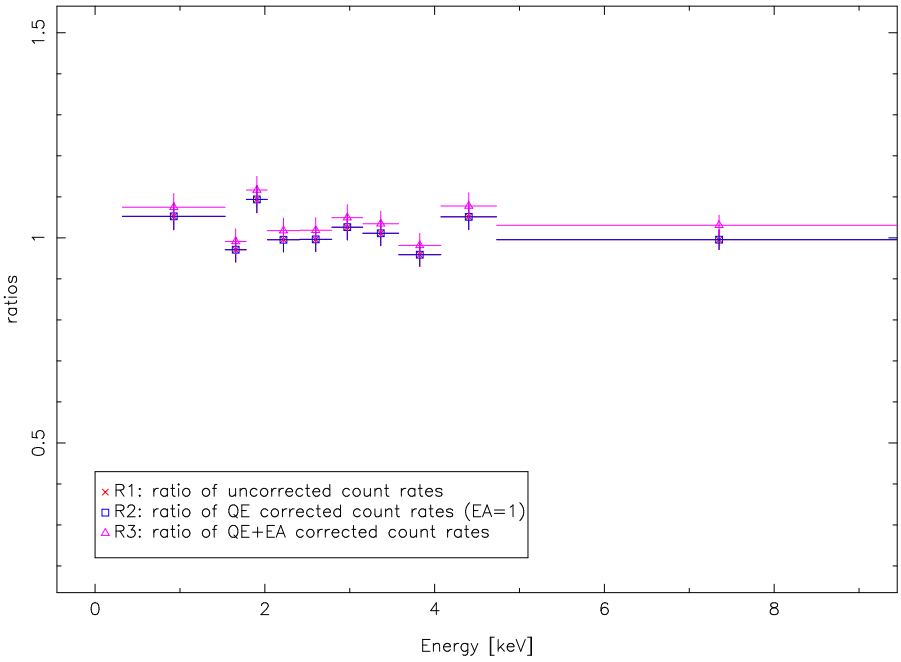

Figure 3: Surface brightness ratios for 2.5′ off-axis. $R_1 \approx R_2$, indicating that the instrumental setup has served its purpose. One would expect R_3 to be unity for an accurate vignetting correction. Energy bands were chosen to provide constant S/N for each band, creating a relatively meaningless band from ∼4.7 to 9.9 keV.

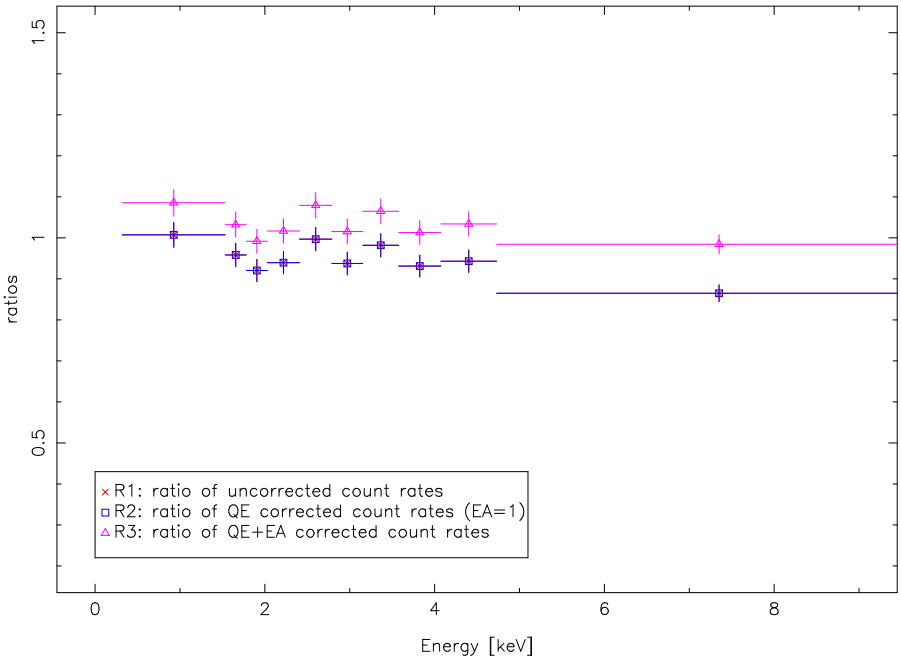

Figure 4: Surface brightness ratios for 5.2′ off-axis.

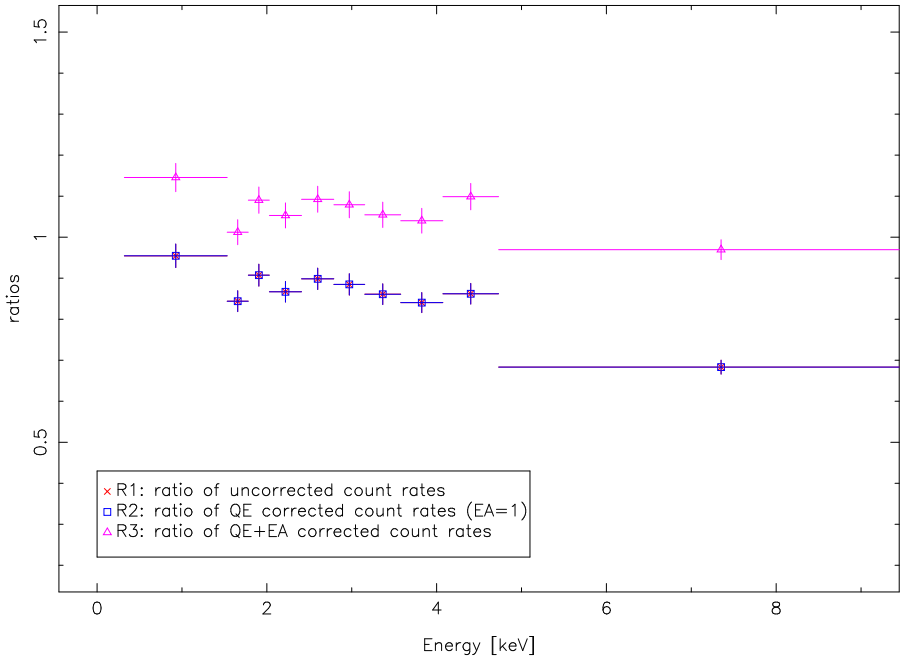

Figure 5: Surface brightness ratios for 10.2′ off-axis.

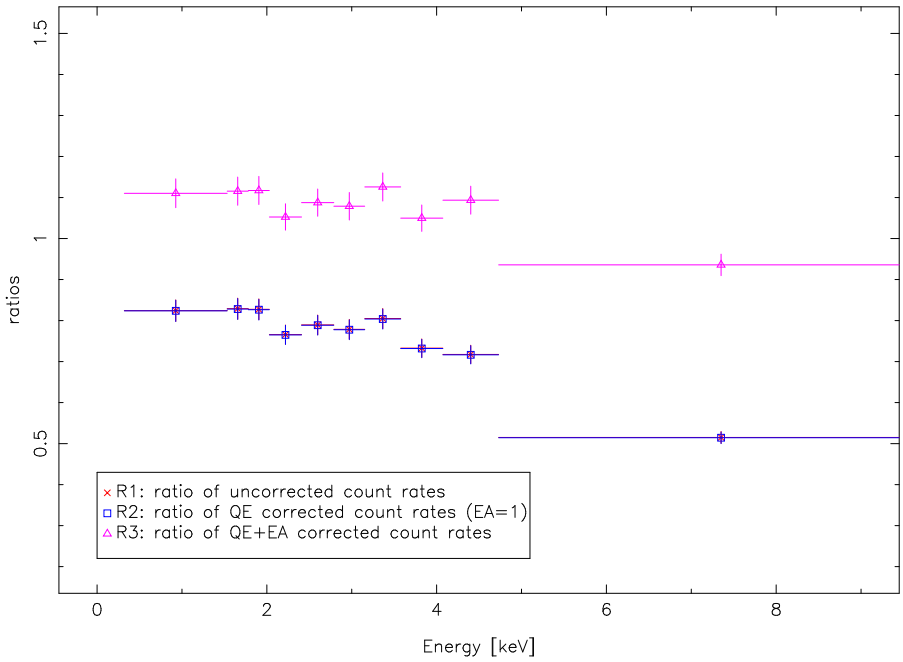

Figure 6: Surface brightness ratios for 15.1′ off-axis.

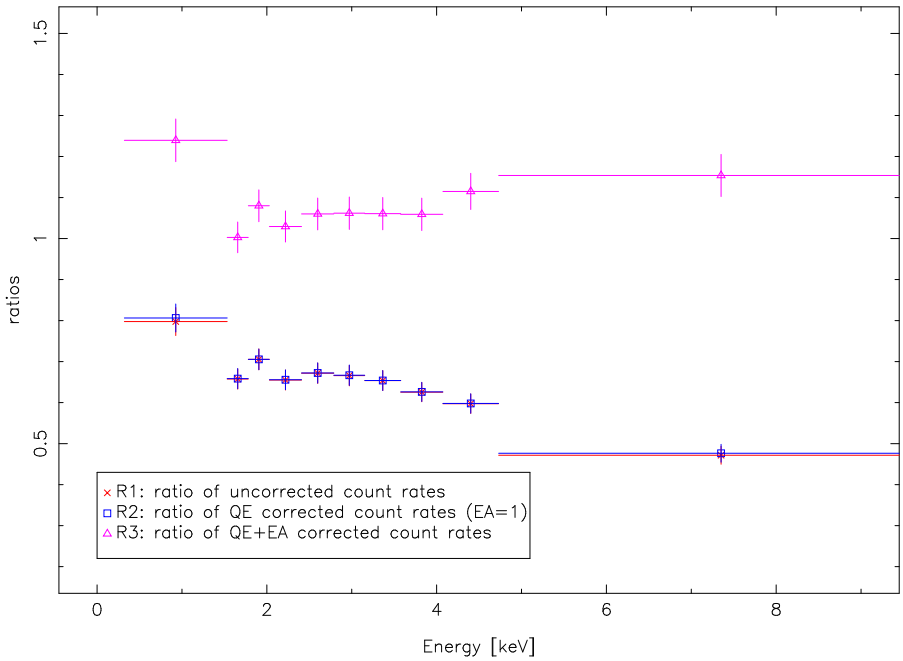

Figure 7: Surface brightness ratios for 20.1′ off-axis. This observation, which did suffer from a background flare, shows some small differences between QE-corrected flux ratios (R_2) and those of the raw count rates (R_1).

References

[1] B. Biller, D. Jerius, Measurement of Vignetting from G21.5 Observations, 11 July 02
`http://cxc.harvard.edu/cal/Hrma/off_axis_effarea/G21.5_data-20020717.ps`